

Extending the Conversion Rate of Sulfur Infiltrated into Microporous Carbon in Carbonate Electrolytes

María L. Para,^[a] Cecilia A. Calderón,^[a] Sara Drvarič Talian,^[b] Florent Fischer,^[c] Guillermina L. Luque,^[d] Daniel E. Barraco,^[a] Ezequiel P. M. Leiva,^[d] and Robert Dominko^{*[b, e, f]}

Infiltration of sulfur into microporous carbon enables the use of carbonate-based electrolytes due to the formation of a compact cathode electrolyte interface. Passivation of the surface prevents direct contact between electrolyte and sulfur. Consequently, the mechanism of sulfur conversion is changed to a quasi-solid-state mechanism with a single sloping plateau related to sulfur conversion in the narrow pores. The narrow size of pores determines the overall pore volume of the microporous carbon and with that sulfur maximum ratio within carbon-sulfur composite. Additionally, a confinement of sulfur in the narrow pores has an impact on sulfur conversion into $\text{Li}_2\text{S}_2/\text{Li}_2\text{S}$ due to volumetric changes when sulfur is reduced. In

this work, we show that the degree of the conversion of sulfur into end discharge products can be extended by lowering the cutoff potential during the discharge process. A higher degree of conversion process causes cracks in the carbon structure enabling a significant increase of capacity while a compact and flexible passivation layer prevents contact with the electrolyte. Quasi solid-state reduction of sulfur is kinetically more favored compared to the consequent oxidation process. Electrochemical impedance spectroscopy measurements show diffusional restrictions in the lower part of the discharge curve that can be correlated with hindered transport due to volumetric changes caused by the reduction of sulfur into $\text{Li}_2\text{S}_2/\text{Li}_2\text{S}$.

Introduction

The worldwide expansion of electromobility and renewable energy sources demands cheap, sustainable powerful energy

storage devices with higher capacity. Lithium-sulfur batteries (LSBs) are being considered a strong candidate to replace lithium-ion batteries (LIBs) since their theoretical energy density (3745 Wh kg^{-1} and 2800 Wh L^{-1}) is three times higher than the state-of-the-art LIBs.^[1-4] Also, sulfur as an active material is cheaper and more sustainable than the current materials of LIBs that use Co and Ni.^[5]

However, before LSBs would have an effective commercial application some issues need to be solved. During battery cycling, S_8 is reduced to form electroactive polysulfides (PS), which are soluble in most of the electrolytes used for LSBs. Long-chain PS diffuse towards the metallic anode where they are reduced to short-chain PS or to insoluble precipitates in form of $\text{Li}_2\text{S}_2/\text{Li}_2\text{S}$. These insulating species contribute to the passive layer formation, resulting in the consumption of active material. Soluble PS furthermore contributes to a poor coulombic efficiency through the shuttle effect, where during charging (oxidation process) long-chain PS are partially or completely reduced on the surface of metallic lithium. This phenomenon is responsible for, progressive loss of active material with cycling, and deactivation of the cell, which results in a short life cycle of the battery.^[6,7] Additionally, S_8 and Li_2S possess low electronic conductivity, which can be mitigated by the addition of carbon with pore volume higher than $1 \text{ cm}^3 \text{ g}^{-1}$. Such porous carbon can sustain a volume expansion of 80% during reduction of sulfur to Li_2S .^[8,9]

Porous carbon materials possess good stability, non-toxicity, excellent compatibility with the electrolyte; they can even be prepared from biomass waste.^[10,11] Porous carbon materials used for LSBs are usually engineered with high specific surface area (SSA) to improve sulfur utilization; enough space to accommodate sulfur and its volumetric expansion and

[a] Dr. M. L. Para, Dr. C. A. Calderón, Prof. D. E. Barraco
Instituto Enrique Gaviola (IFEG), CCT Córdoba-CONICET
Facultad de Matemática, Astronomía y Física
Universidad Nacional de Córdoba (UNC)
Av. Medina Allende s/n, Ciudad Universitaria, 5000 Córdoba, Argentina

[b] Dr. S. Drvarič Talian, Prof. R. Dominko
National Institute of Chemistry
Hajdrihova 19, SI-1000 Ljubljana, Slovenia
E-mail: Robert.Dominko@ki.si

[c] Dr. F. Fischer
Florent Fischer, SAFT, Research & Technology
111 boulevard Alfred Daney, 33074 Bordeaux, France

[d] Dr. G. L. Luque, Prof. E. P. M. Leiva
Instituto de Investigaciones en Físico-química de Córdoba (INFIQC) CCT
Córdoba-CONICET
Facultad de Ciencias Químicas
Universidad Nacional de Córdoba (UNC)
Haya de la Torre y Av. Medina Allende, Ciudad Universitaria, 5000 Córdoba, Argentina

[e] Prof. R. Dominko
University of Ljubljana
Faculty of Chemistry and Chemical Technology
Večna pot 113, SI-1001 Ljubljana, Slovenia

[f] Prof. R. Dominko
ALISTORE – European Research Institute
33 rue Saint-Leu, 80039 Amiens, France

 Supporting information for this article is available on the WWW under
<https://doi.org/10.1002/batt.202100374>

 An invited contribution to a Special Collection dedicated to Lithium-Sulfur Batteries.

 © 2022 The Authors. *Batteries & Supercaps* published by Wiley-VCH GmbH. This is an open access article under the terms of the Creative Commons Attribution License, which permits use, distribution and reproduction in any medium, provided the original work is properly cited.

proper pore size to retain intermediate products.^[8] Although these materials have led to high capacities and good cyclability, the carbon matrix by itself is not effective enough to avoid the shuttle effect and capacity fading cannot be stopped by the use of mesoporous carbon. Other strategies, as the development of adsorption additives,^[12] ionoselective separators,^[13,14] or the use of carbon materials with a designed porosity,^[15,16] are used to retain polysulfides on the cathodic side of the LSB.

The nucleophilic nature of PS prevents the use of carbonate-based electrolytes (CBE) in the LSB and the most used are ether-based electrolytes (EBE).^[17] The reaction mechanism in EBE is based on the solid-liquid-solid transformation of sulfur through the soluble PS with end mixture typically in the form of mixed solid Li_2S_2 – Li_2S phases. The solid-liquid-solid transformation has well characteristic two potential plateaus.^[4,18–20]

The strategies to improve the LSB performance are focused on the suppression of PS dissolution or catalytic transformation of sulfur into end discharge products with low solubility. Ultramicroporous carbons are very interesting materials due to their very narrow pores. The sulfur is confined inside the pores with a narrow diameter smaller than 1 nm. That represents a barrier for solvation and dissolution and it has impact on the sulfur conversion mechanism.^[20–22] Theoretical studies predict that only small sulfur molecules have the appropriate size to accommodate in pores with the size below 1 nm, while long-chain PS are less likely to be formed inside so narrow pores.^[23] Nevertheless, there are some experimental studies where long-chain PS species were detected.^[20] Sulfur confinement and the formation of cathode electrolyte interface (CEI) on the surface of ultramicroporous carbons allow the use of CBE. Once the CEI is formed, lithiation-delithiation reactions occur through a quasi-solid-state mechanism, which is evident in the potential/capacity profile through the appearance of only one ill-defined plateau.

In this work, we explore the electrochemical behavior of a sulfur-ultramicroporous composite with CBE. We study the dependence of the electrochemical behavior by changing the low cut-off potential window. We show that a decrease of cut-off potential improves the utilization of active material while not affecting the cycling stability. The formation of SEI on the sulfur-ultramicroporous composite proceeds during the first reduction polarization and it competes with sulfur conversion. Once SEI is formed on the surface, a sulfur-ultramicroporous composite can be even cycled in ether-based electrolytes without any degradation.

Results and Discussion

Active material characterization

The (BET) specific surface area (SSA), micropore volume (μPV) and total pore volume (TPV) for MC material are $3108 \text{ cm}^2 \text{ g}^{-1}$, $0.160 \text{ cm}^3 \text{ g}^{-1}$ and $1.74 \text{ cm}^3 \text{ g}^{-1}$, respectively (Table S1). According to these values, the maximum amount of sulfur that could be hosted in MC is 78 wt% of sulfur. We have selected a mass

ratio 3:2 of S:C for the preparation of the active material.^[2] After sulfur infiltration, the SSA, μPV and TPV of MC–S decreased to $347 \text{ cm}^2 \text{ g}^{-1}$, $0.005 \text{ cm}^3 \text{ g}^{-1}$ and $0.21 \text{ cm}^3 \text{ g}^{-1}$, respectively (Table S1). These remarkable reductions are attributed to the incorporation of sulfur into the pores of MC. XRD pattern (Figure S1) shows no sulfur peaks, indicating there is no crystalline sulfur on the MC–S composite surface. The morphologies of MC and MC–S composite were studied using SEM as shown in Figure S2. There is no significant difference between both samples, big particles with smooth surface and layered structure can be seen, which indicates the sulfur is incorporated inside of the pores. Elemental analysis showed that the amount of sulfur in the composite after infiltration was 56.5 wt%.

Electrochemical characterization

Figure 1 shows the CV and galvanostatic cycling response for MC–S in a CBE. Two cathodic peaks at 2.2 and 1.4 V appear in the first CV cycle (Figure 1a), while the following cycles present only one cathodic peak at 1.7 V. The potential response during galvanostatic cycling is plotted in Figure 1(b and c). The discharging profile for the first cycle (Figure 1b, black continuous line) shows two potential plateaus at ~2.3 and 1.6 V, respectively, while the first charging profile shows a unique potential plateau at ~2.4 V. For the following discharge cycles (Figure 1b and c) there is only one potential plateau at 1.7 V. The presence of two processes in the first discharge and one on the following discharges is in the agreement with CV results (Figure 1a). According to the literature, the first cathodic peak at ~2.4 V corresponds to the conversion of sulfur leftover on the surface and the second at 1.7–1.6 V is associated with sulfur conversion in the pores and CEI formation.^[20,24] The unique process observed during the discharge for the following cycles is assigned to the S_8 reduction and formation of PS and Li_2S_2 / Li_2S through a quasi-solid-state mechanism (QSS), without the occurrence of any soluble PS in the electrolyte.^[20,25–28] Specific capacity and coulombic efficiency (CE) versus cycle number are plotted in Figure 1(d). During the first cycles, the CE is low but increases monotonically, reaching 99% after 15 cycles. After the slight increase of specific capacity in the formation cycles, the capacity retention is stabilized.

To study the formation of the CEI during the first reduction process, we have prepared several MC–S cells which were cycled at galvanostatic conditions between 3.0 V and different cutoff potentials (E_f), where E_f changes after three cycles (Figure 2a and b). Selected cutoff potentials are following: 1.8, 1.6, 1.3, 1.0 and 0.5 V. An increase in the discharge capacity is observed whenever E_f decreases (black asterisks in Figure 2a). Although this behavior is expected due to a more negative potential window, the difference between discharge and charge capacity indicate that part of the charge used in the reduction process is consumed for irreversible processes related to the CEI formation.^[24,29–31] The potential/capacity response for the different cutoff potentials is shown in Figure 2(b). The potential plateau at ~2.4 V appears only during the first discharge cycle (Figure 2b, 1st cycle – black line, $E_f = 1.8 \text{ V}$). The

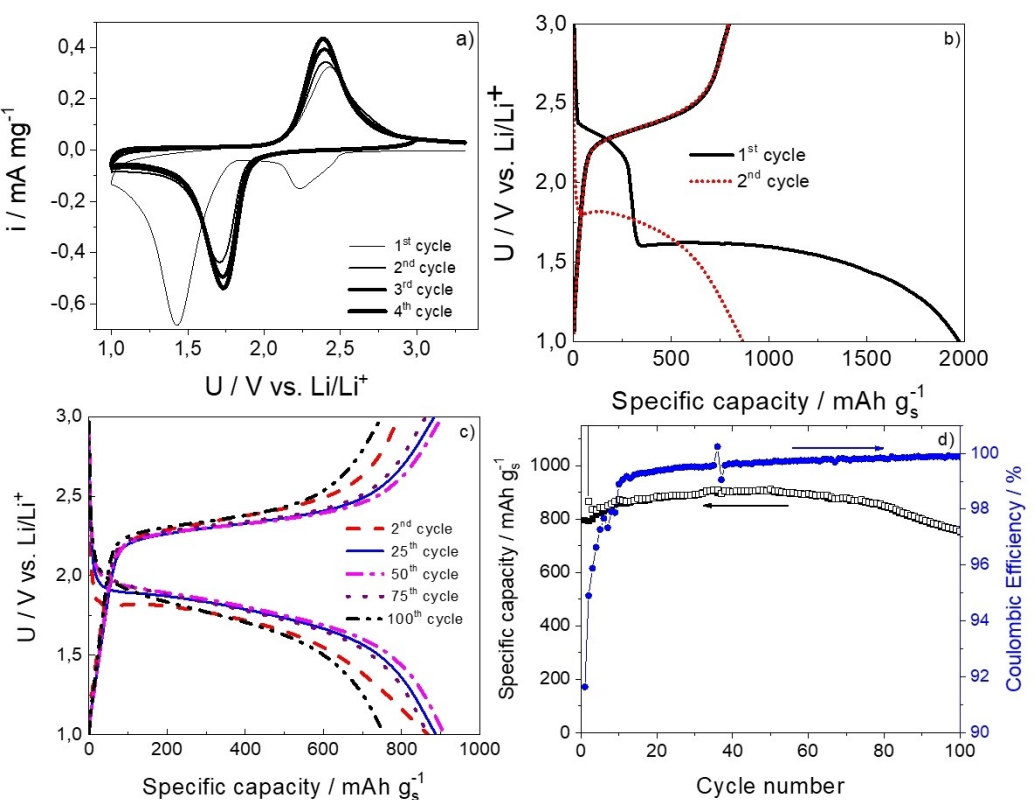


Figure 1. MC–S electrode with CBE. a) Cyclic voltammetry at 0.05 mV s^{-1} ; b) and c) selected galvanostatic curves, d) capacity and CE evolution with cycle number at 0.2 C .

following cycles do not show any electrochemical activity at this potential, confirming our assumption that the electrochemical signature at $\sim 2.4 \text{ V}$ is related to the reaction of sulfur leftover on the outer side of the pores. Decreasing the cut-off voltage to $E_f = 1.6 \text{ V}$ (Figure 2b, 4th cycle – red line) the capacity increases sharply and 60% of the charge is not recovered on the next charge step, therefore this charge is preferable consumed for the CEI formation. In the first cycle with a cutoff potential of $E_f = 1.3 \text{ V}$ (Figure 2b, 7th cycle – blue line) a mixed behavior appears: one plateau at 1.7 V for QSS sulfur-lithium reaction and a second plateau at 1.5 V , associated with CEI formation.^[32] For the $E_f = 1.0$ and 0.5 V the electrochemical behavior is stabilized with a unique potential plateau at 1.7 V and extra irreversible charge due to CEI formation just for the first cycle at each potential interval (Figure 2b, 10th cycle and 13th cycle – pink and orange lines, respectively). Capacity remains stable for cycling between 3.0 – 0.5 V (Figure 2a). Results shown in Figure 2(a and b) show mixed reaction mechanism related to the consumption of available sulfur on the surface above 2 V , formation of CEI and QSS sulfur-lithium reaction in the voltage region between 1.3 and 1.7 V . Decrease of cut-off voltage to lower value contributes a minor part of the irreversibility in the formation cycles. Further study of how E_f influence capacity retention and battery stability are shown in Figure 2(c and d). Here we changed the cut-off potential from 1 V to 0.5 V and 0.25 V . Figure 2(c) shows results for an MC–S electrode cycled between 3.0 and E_f which was decreased every 5 cycles to lower cut-off value and at the end followed by

extended cycling between 3.0 and 1.0 V . As previously observed, two potential plateaus appear in the first discharge of the electrode, at ~ 2.4 and 1.6 V (Figure 2d, 1st cycle – black line) and for the following cycles only one potential plateau window at 1.7 V is obtained what is in the agreement with a QSS reaction mechanism. Additional irreversibility in the first cycle is observed when we decrease the cut-off potential to $E_f = 0.5 \text{ V}$ (6th cycle in Figure 2c – green line in Figure 2d). We observed the increase of capacity for approximately 250 mAh g^{-1} . Additional decrease of the cut-off voltage to $E_f = 0.25 \text{ V}$ (11th cycle in Figure 2c and light blue curve in Figure 2d) corresponds to further increase of specific capacity close to theoretical capacity (1610 mAh g^{-1}), however almost no irreversible loss has been accumulated with this potential change. Returning to the cut-off voltage $E_f = 1.0 \text{ V}$, the specific capacity decreases to 1225 mAh g^{-1} which is an almost a 25% increase of capacity due to activation of material by decreasing the cut-off potential. Cycling in the potential range shows slow but pronounced capacity fading. We speculate that with polarization to lower cut-off voltage, a higher degree of sulfur conversion to $\text{Li}_2\text{S}/\text{LiS}$ phase is obtained. The required volume expansion during sulfur conversion to Li_2S may provoke an expansion of the carbonous matrix resulting in more sulfur electrochemically accessible in the subsequent cycles. Potential degradation of porous structure leading to possible reaction of sulfur with CEI can be expected and that would explain slow capacity fading.

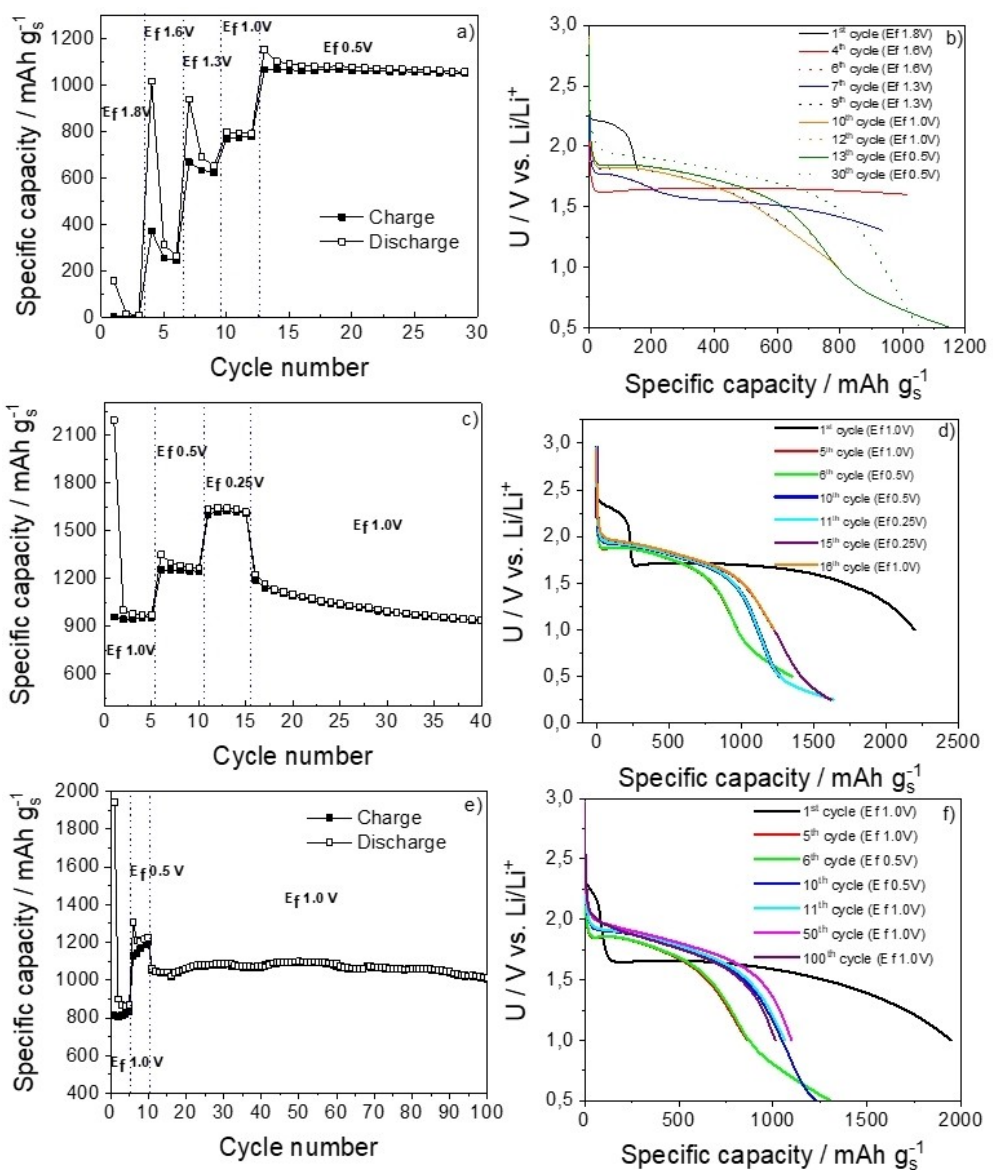


Figure 2. MC–S electrode in CBE: a), c) and e) cycling performance at 0.2 C and b), d) and f) galvanostatic discharge curves for variable cathodic potential cutoff (E_f) that is indicated inside each graph.

To check if cutoff potential of $E_f=0.25$ V is harmful for the composite we performed an experiment where the lowest cut-off potential was $E_f=0.5$ V. The cycling conditions were in the formation cycles set-up to $E_f=1.0$ V for the first 5 cycles, then low voltage cut-off was changed to $E_f=0.5$ V between cycle 6–10 and after 10th cycle cut-off potential was shifted back to $E_f=1.0$ V for the rest of the cycles (Figure 2e) and f). An increase of capacity for 26% have been obtained when we compare 5th and 11th cycles (from 840 to 1060 mAh g⁻¹) which is very similar to observed capacity increase when the lowest cut-off was set to $E_f=0.25$ V, while the capacity stability is significantly improved when cutoff potential in the formation cycles is not below 0.5 V.

To elucidate if the sulfur presence affects CEI formation, electrodes with MC without sulfur were prepared and cycled between 3.0 V and E_f , where E_f equal to 1.0, 0.5 and 0.25 V

(Figure S3). The first discharge with $E_f=1.0$ V shows a unique potential plateau at 1.6 V with an irreversible charge of 530 mAh g⁻¹ (Figure S3b). This process is not present in the following cycles with the same potential interval. On the first discharge with $E_f=0.5$ V and $E_f=0.25$ V an irreversible charge still appears (black and red squares in Figure S3a, respectively) even in the absence of sulfur in the electrode. These results show that a fraction of the irreversible charge observed for MC–S electrodes (Figure 2) is due to the MC contribution to CEI formation. For further cycling between 3.0 and 1.0 V a small capacity of 80 mAh g⁻¹ still appears due to the possibility of intercalation of Li⁺ in the graphitic carbon walls of MC.^[33]

Figure 3 presents SEM images of an uncycled MC–S electrode (Figure 3a) and MC–S electrodes after first discharge with different discharge cut off values (Figure 3b–d). Images for uncycled electrode show particles with a dimension of several

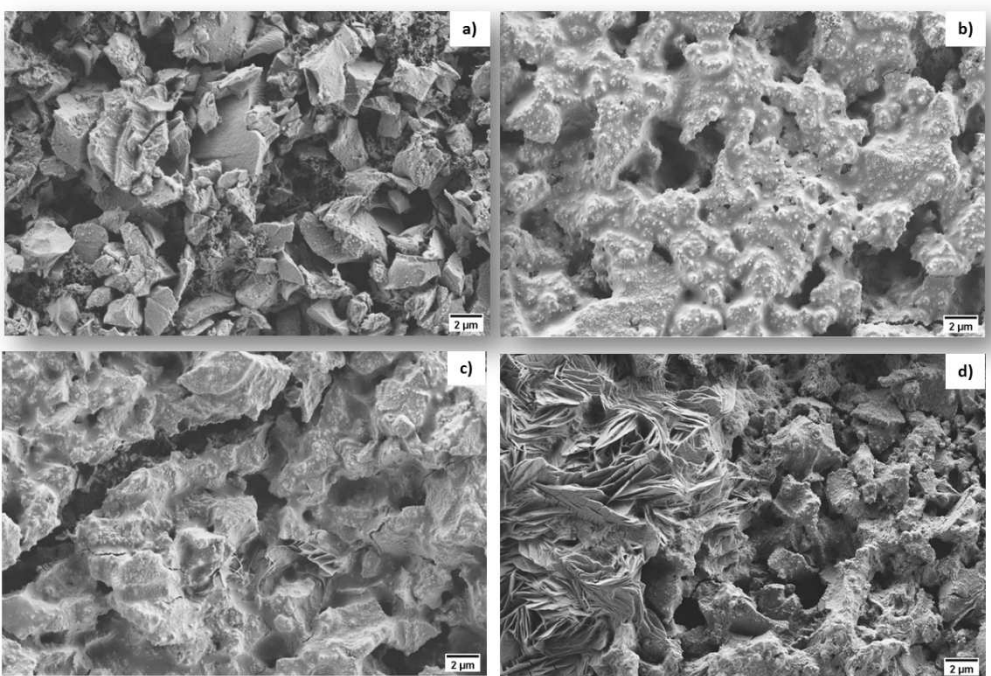


Figure 3. SEM images of cathodes surfaces for a) charged pristine electrode immersed in CBE, discharged electrodes (first cycle) with cut-off potential b) 1.0 V, c) 0.5 V and d) 0.25 V.

micrometers well mixed with conductive additive SEM images for discharged electrodes with E_f 1.0, 0.5 and 0.25 V (Figure 3b, c and d respectively) show the surface of the electrodes covered with a surface film which topography changes with the discharge cutoff voltage. The image for the electrode discharged until $E_f=1.0$ V shows a smooth surface film with some small cracks. The surface film on the electrode discharged until $E_f=0.5$ V becomes rougher and some cracks appear. We correlate crack appearance with formation of higher amount of Li₂S. The surface for the MC-S electrode discharged until $E_f=0.25$ V shows some laminar structures, degradation of the surface film and more cracks.

The results discussed above show that electrodes cycled between 3.0 V and 0.5 V present the highest capacity with stable cyclability. An activation procedure for three cycles at 0.2 C using a low cutoff voltage of 0.5 V has been used for the cells that were further tested for the rate capability (Figure 4). Two types of rate capability tests were done: with constant charging at 0.2 C and discharging at different C-rates (Figure 4a) and with charging and discharging at the same rates (Figure 4b). The cutoff potential was setup to 1 V after the initial 3 cycles. In both cases, the initial C-rate cycling was performed at 0.2 C to set a reference capacity value. The corresponding galvanostatic curves presented in Figure S4 show the evolution of capacities and polarization at different

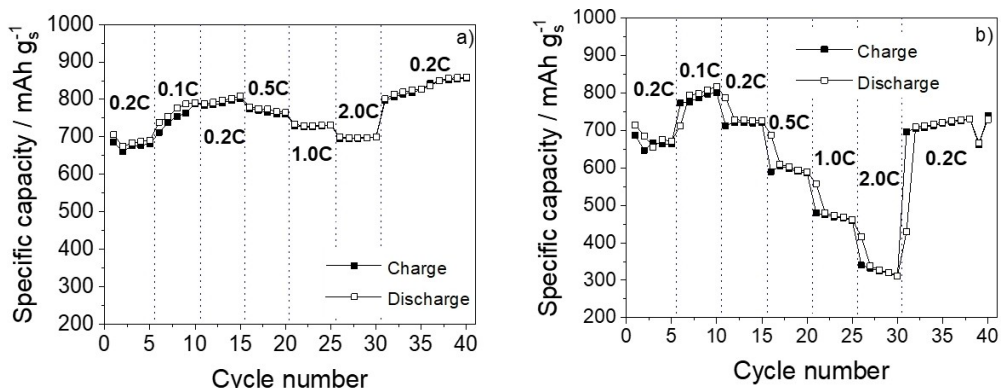


Figure 4. MC-S Rate capability experiments with electrodes previously cycled 3 times between 3.0 and 0.5 V (not included on the graph): a) electrodes charged at constant 0.2 C and discharged at different current densities and b) electrodes charged and discharged at different current densities (indicated as a c-rate in the figure).

current densities during discharge. Polarization increase is very similar in both measurements while the capacity drop is much more significant in the case of cycling regime where same current densities were used for discharge and charge. The rate capability experiment with a constant charging rate of 0.2 C (Figure 4a) shows a continuous increase in capacity until discharge rate of 0.5 C, reaching the maximum value of 808.7 mAh g^{-1} for 0.2 C discharge rate. For discharge rate of 0.5 C, 1.0 C and 2.0 C capacity slightly decrease to 779.7, 733.9 and 699.5 mAh g^{-1} , respectively. Moreover, for rate capability where charging rates are equal to discharging rate the drop in capacity is significantly higher (Figure 4b). Every time the rate increases the capacity drops, reaching the lowest value of 310.0 mAh g^{-1} at 2 C rate. This shows that an MC–S electrode can deliver much higher power during discharge (sulfur reduction), while the kinetics of the oxidation of lithium sulfide or lithium polysulfides is much slower. A possible explanation can be derived from the work published by Cheon et al. who found that the final part of the discharge on a Li–S electrode is where capacity is most affected by the increase in current density reaction because of Li_2S formation.^[34] Conversion from Li_2S to Li_2S_2 (and vice versa) has sluggish kinetics since a solid–solid equilibrium is involved.^[35] When this reaction is the initial

one (charging step) capacity becomes more sensitive to the current density increase, limiting the amount of sulfur that reacts.

The results discussed above unequivocally show that MC–S discharge occurs via a QSS mechanism, and it agrees with our previous paper where we published a mechanism of sulfur conversion by using XAS.^[20] This is in the agreement with other papers^[24,29–32] where different groups came to the same conclusion. The formation of CEI in the starting cycles prevents the direct contact between CBA and sulfur, while lithium diffusion through interface enables a reversible conversion of sulfur to Li_2S .^[21] To test the compactness of the CEI, an MC–S electrode was cycled in CBE for 160 cycles, washed and transferred to a new fresh cell, and cycled using ether-based electrolyte (EBE). Figure 5 shows the capacity evolution with cycle number, the continuity between the CBE cycles (black) and the EBE cycles (red) curves is remarkable, both in capacity and coulombic efficiency. The cathode is highly stable during further 40 cycles in the new electrolyte (EBE) what can be observed from the galvanostatic profiles for cycles on CBE and EBE which are shown as insets in Figure 5, respectively. When the electrode cycled in CBE is transferred to a new cell and cycled with EBE, the potential profile stills shows a unique

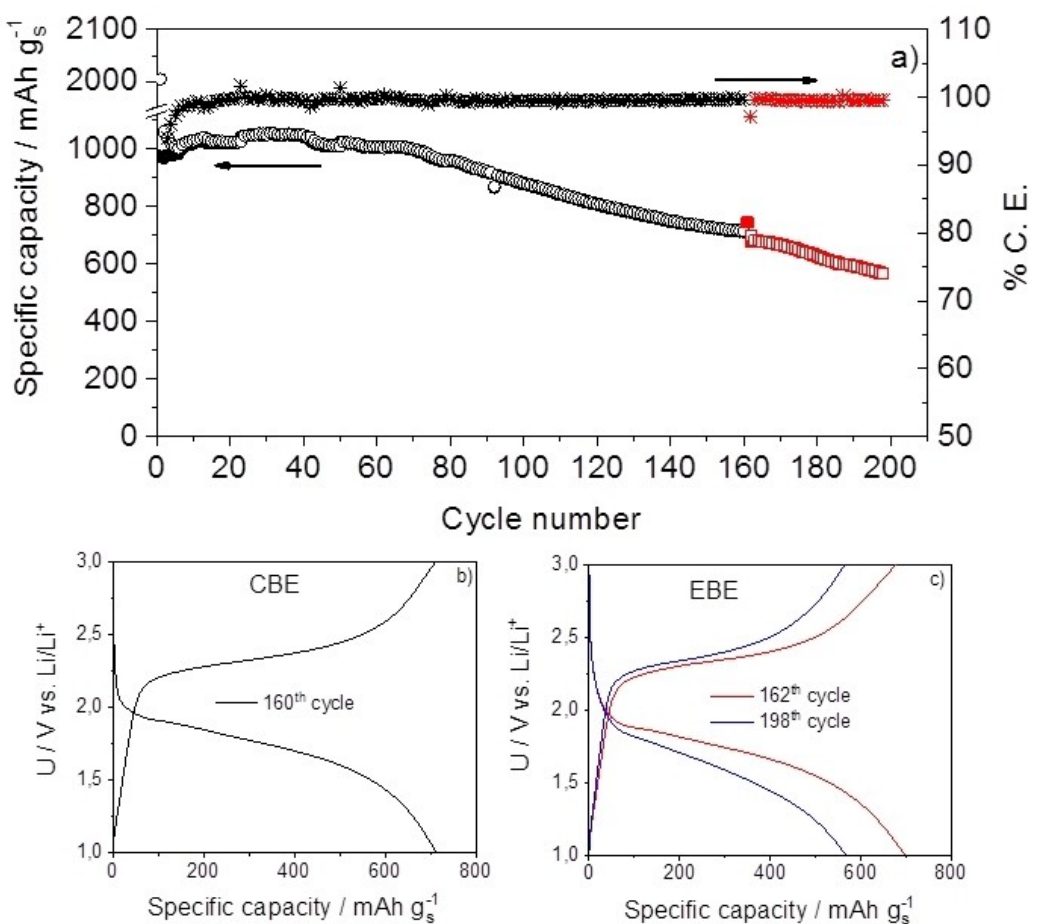


Figure 5. a) Capacity and CE evolution with cycle number for cycling in CBE (black symbols) and EBE (red symbols) at 0.2 C. Galvanostatic curves for b) cycle 160 on CBE and c) cycles 162 and 198 on EBE.

signature of ill-defined single plateau conversion consistent with a QSS mechanism. The potential discharge profile for an MC-S electrode cycled in EBE from the first cycle (Figure S5) shows two potential plateaus according to a solid-liquid-solid reaction mechanism.^[4,36,37] The change in the mechanism of the electrode cycled in EBE when this electrode is previously cycled in CBE is an evidence that the CEI formed is responsible for the change of the reaction mechanism leading to reduction-oxidation of sulfur confined to the pores. Also, the formed CEI is stable even in EBE keeping sulfur confined inside the pores.

The operation of the MC-S cathode with CBE was evaluated using electrochemical impedance spectroscopy (EIS). Figure 6 shows the experimental data, which were obtained by discharging the cell at 0.2 C, stopping the current every thirty minutes for a 15 min period of relaxation and subsequently measuring impedance spectra at OCV. The voltage curve is shown in Figure 6(a). The curve shows spikes due to the relaxation periods, while the points of EIS measurements are labeled with dots. Disregarding the relaxation spikes and impedance measurement dots, the curve closely resembles the galvanostatic response of the cell usually obtained in the first discharge (see Figures 1 and 2). A characteristic impedance spectrum for the cell is shown in the inset of the Figure 6(b). It has at least four different distinctive contributions: i) the electrolyte resistance, ii) Li SEI resistance (300 Hz arc), iii) a small middle frequency arc (2 Hz) and iv) a low-frequency tail. There

are likely several other impedance features also present in the impedance response, yet they are merged or too small to be distinguished.

Calculating from the value of the relaxation voltage (difference between the galvanostatic curve and EIS OCV measurement point), which is roughly 0.3 V, the expected impedance contributions should be in the size order of 1 to 2 k Ω . Considering this, the size of the impedance features in some of the measured spectra is exceedingly large. See for example the first three spectra in Figure 6(e), which show considerably larger impedance, reaching up to 10 k Ω . This low-frequency arc has capacitance around 0.01 F, which corresponds well to the capacitance associated with the total surface area of the microporous carbon cathode matrix. Taking this into account together with a significant decrease of the feature when the cell is under load suggests that this contribution could be connected to the charge transfer process.

The change due to decreasing the SOC can be monitored both through observing the differences in the relaxation voltage curves (Figure 6c) and through the evolution of the impedance response (Figure 6d and e). The relaxation curves can be regarded as an approximation of a GITT experiment, with the difference being that here, the relaxation was stopped after 15 min, while in the usual GITT experiment, the OCV period is stopped after the potential change is sufficiently small (e.g., a limit of 15 mVh $^{-1}$). Figure 6(c) shows the normalized

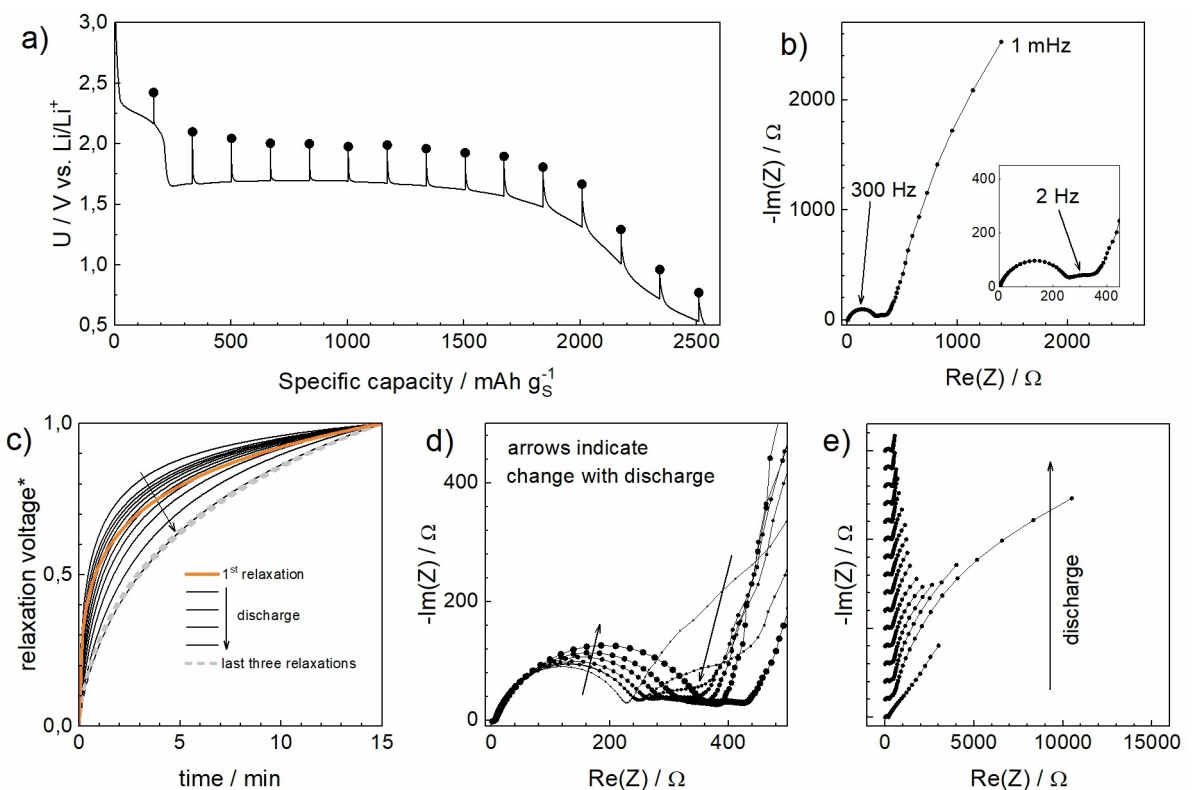


Figure 6. Impedance spectroscopy experiment during the first discharge of a MC-S cathode cell with CBE: a) potential change during the experiment, the dots show the points of impedance spectroscopy measurements; b) a typical impedance spectrum measured, c) relaxation voltage curves during discharge; d) magnification of the high and middle frequency region of impedance spectra change during discharge; e) full impedance spectra measured during discharge. *The absolute values of the voltages are normalized.

voltage curves for all the relaxation periods during the first discharge of the cell from Figure 6(a). The first relaxation curve is different from the subsequent ones and it does not follow the same trend. This is expected, since it belongs to an entirely different process happening at higher voltages in the first short plateau. The following relaxation curves show a gradual evolution towards slower relaxations, which indicate that slower, low-frequency processes (likely some form of diffusion) are becoming more constrictive for the operation of the cell. This same change is not readily distinguishable from the impedance spectra evolution (Figure 6e), most likely due to being hidden behind the before-mentioned impedance features due to charge transfer reactions. There is, nevertheless, an evident decrease of the small middle-frequency arc (Figure 6d), which fits in with the general direction of change observed in relaxation curves. The last four relaxation curves practically overlap (grey dashed curves in Figure 6c). These were measured in the lower voltage sloping region of the galvanostatic curve, where the potential is continuously shifting. This suggests an additional process taking place in the lower voltage regions. To explain – if we presume that only a single electrochemical process takes place in the cell after the start of the lower voltage plateau until the cell reaches the discharge voltage cut off, then we would expect the relaxation curves to mimic this by slightly, yet continuously changing. In the last section of the first discharge, it is evident that the potential of

the cell starts decreasing (sloped region after approx. 1800 mAh g^{-1}). If we assume that this is the effect of an increase in overpotential producing a deviation from an otherwise flat voltage plateau (the same one as throughout the lower voltage plateau region), then the relaxation curves are expected to also change in this same direction. Since the relaxation curves remain identical, this suggests that the thermodynamic potential of the cell also changes, which can be explained by an additional process taking place.

The same experiment was continued through the next cycle of cell operation (Figure 7). The relaxation potentials (dots in Figure 7a) again indicate a second low voltage plateau process associated with a large hysteresis between discharge and charge. The relaxation voltages (Figure 7b and c) as well as impedance spectra shape change during discharge (Figure 7e and f) is the inverse of change during charge. In comparison with the first discharge (Figure 6), the general shape of the spectra changes slightly in the high-frequency region (see inset on Figure 7e). This change indicates that the Li metal anode contribution is significantly decreasing. This phenomenon has been associated with the formation of high surface area lithium/dendrites on the anode, changing the electrode's nature from flat to porous, and consequently producing the evidenced impedance features (the reader is directed to Ref. [38] for further information). The high-frequency arc at low SOC (Figure 7d). This arc decreases again on subsequent

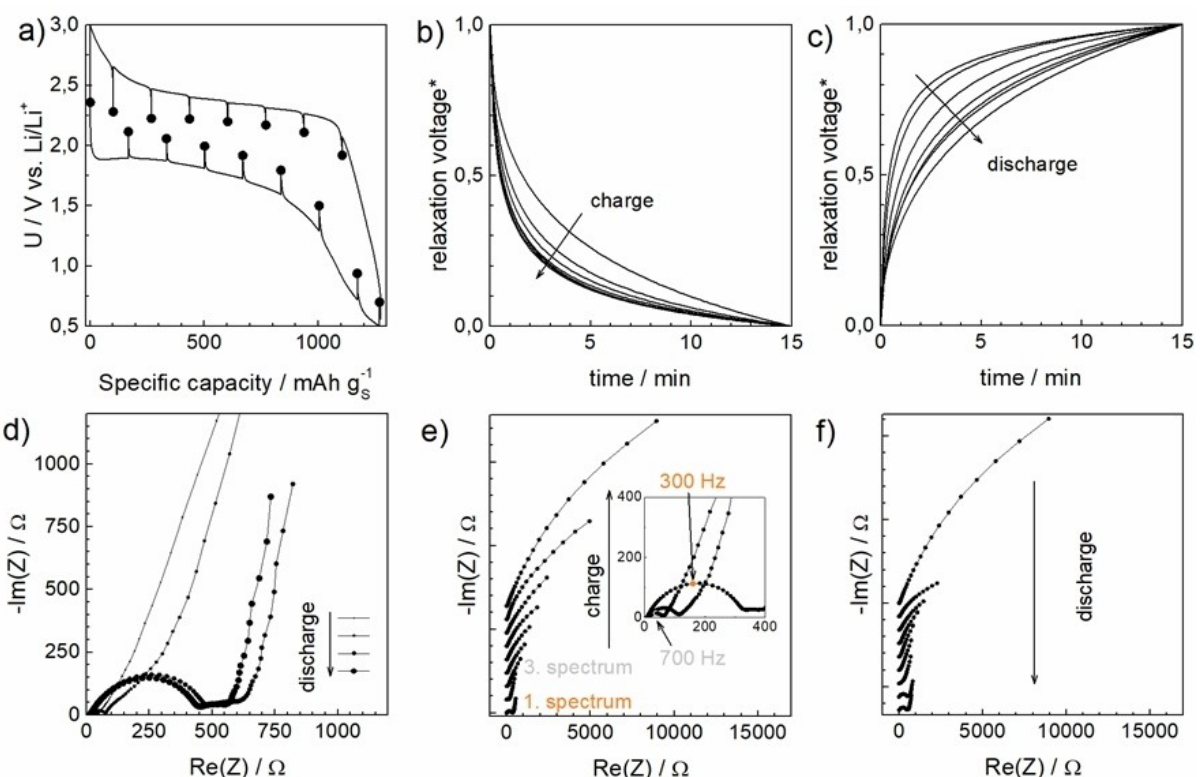


Figure 7. Impedance spectroscopy experiment during the second cycle of a MC-S cathode cell with CBE: a) potential change during the experiment, the dots show the points of impedance spectroscopy measurements; b) and c) relaxation voltage curves during charge and discharge, respectively; d) magnification of the high and middle frequency region of impedance spectra change during the end of discharge (last four spectra measured); e) and f) full impedance spectra measured during charge and discharge, respectively.

charging (not shown). Through a symmetrical cells experiment (Figure S6) it was determined that this feature belongs to the lithium metal anode and can be explained by a decrease of the initially available high surface area lithium decreasing through the process of stripping taking place on the lithium metal anode during discharge.

Impedance spectroscopy studies therefore show that the spectra measured at OCV include a large contribution, which is most likely associated with the charge transfer reaction. The experiment also discerned the variation in the lithium metal anode contribution at high frequencies, which decreases during charge (formation of high surface area lithium) and increases during discharge (consumption of the high surface area lithium).

Conclusion

In the present work, we show the electrochemical performance of ultramicroporous carbon with infiltrated sulfur in CBE. MC–S electrodes cycled with CBE show large reduction capacities in the formation cycles that are connected with a CEI formation process and with a QSS reaction mechanism. The electrochemical behavior of the electrode depends on discharge cut-off voltage during the formation cycles. An increase in capacity was found when the electrodes were discharged to potentials of 0.5 and 0.25 V vs. Li/Li⁺. This is attributed to a conversion ratio of sulfur to the Li₂S₂ and Li₂S phases, which generate an expansion enabling higher conversion in the continuous cycling. However, the stability of cycling is affected with a cutoff potential since electrode cycled to 0.25 V suffers a loss of capacity with cycling, which indicates possible damages in the structure of the carbon host matrix and/or in the composition of the CEI. In addition, the rate capability of this material shows that the capacity is more sensitive to the current density applicable for charging. Impedance spectroscopy shows large importance of charge transfer reaction process. It was shown that the typical SLS reaction mechanism of an MC–S electrode cycled in EBE can be changed to a QSS mechanism when the electrode is previously cycled in CBE due to the protective CEI formed in the carbon-based electrolyte. This proves not only the key role that the CEI plays in the lithiation reaction mechanism and avoiding capacity loss, but also that this CEI is chemically stable.

Experimental Section

Active material preparation

Elementary sulfur (Sigma Aldrich) without any previous purification and microporous carbon (MC) provided by SAFT Company (France) were manually mixed in a proportion of 3:2 in weight, respectively. The prepared mixture was heated to 155 °C for 5 h followed by 30 min at 300 °C with a 0.2 °C min⁻¹ heating ramp in a sealed evacuated vessel to obtain the active material (MC–S). The final S content was determined by elemental analysis (CHNS).

Characterization techniques

Scanning electron microscopy images were taken by using a field-emission scanning electron microscope (FE SEM Supra 35 VP Carl Zeiss) equipped with an energy dispersive X-ray spectrometer INCA Energy 400 (Oxford Instruments). Samples were prepared inside an argon-filled glovebox and transferred in a custom-made vacuum transfer holder to avoid contamination with the atmosphere. X-ray diffraction was measured in the quartz capillary by using PANalytical X'Pert PRO (CuK_{α1} I ¹/₄ 1.5406 Å) diffractometer. Nitrogen adsorption measurements were carried out at 77 K on a Tristar 3000 Micromeritics volumetric adsorption analyzer. The samples were outgassed under vacuum for 2 h at 473 K before the adsorption analysis. Specific surface areas were determined from the Brunauer–Emmett–Teller (BET) method.

Electrochemical measurements

MC–S electrodes were prepared by mixing MC–S active material, poly(vinylidene fluoride) (PVDF), and carbon black C65, in a ratio of 8:1:1 weight respectively, with N-methylpyrrolidone (NMP) as solvent. The obtained slurry was casted onto carbon-coated aluminum foil as a current collector. Electrodes with a surface area of 1.13 cm² and sulfur loading between 0.7–1.0 mg of sulfur per cm² were cut and dried at 50 °C overnight. Coin cells CR2032 assembled inside an argon-filled glove box with a manual crimper (Hohsen Corporation) were used for electrochemical characterization and were disassembled with a coin cell disassembling tool (Hohsen Corporation) for the post-mortem analyses. All cells were assembled using Celgard 2320 as a separator and a metallic lithium disc (1.13 cm² surface and 110 μm thickness) as counter-electrode. Solutions of 1 M lithium hexafluorophosphate (LiPF₆) in fluoroethylene carbonate (FEC): dimethyl carbonate (DMC) (v/v – 1:4) (from now on called CBE) mixture and 1 M lithium bis(trifluoromethanesulfonyl)imide (LiTFSI) in 1,3-dioxolane (DOL): dimethyl ether (DME) (v/v – 1:1) mixture were used as electrolytes with 40 μL mg⁻¹ ratio.

Cyclic voltammetry (CV) experiments were done between 3.0 V and 1.0 V vs. Li/Li⁺ at 0.05 mV s⁻¹ scan rate starting at open circuit voltage (OCV) to cathodic scan. Electrochemical impedance spectroscopy (EIS) measurements were done in the potentiostatic mode at OCV with 10 mV of amplitude (rms) between 1 MHz and 1 mHz. CV, using Biologic VMP3 or MPG2. Galvanostatic cycles were done at 0.2 C current density (except for C rate experiments) between 3.0 and 1.0 V vs. Li/Li⁺ (except for cathodic cut-off potential effect experiments) in a MACCOR 4200 galvanostat/potentiostat station.

Acknowledgements

M. L. P. and C. A. C. thank CONICET-Argentina for the “young researchers” scholarship. This work was supported by the HELIS project which receives funding from the European Union’s Horizon 2020 research and innovation program under Grant Agreement No 666221 and from the Slovenian Research Agency research program P2-0393.

Conflict of Interest

The authors declare no conflict of interest.

Data Availability Statement

The data that support the findings of this study are available from the corresponding author upon reasonable request.

Keywords: carbonate electrolyte • cathode-electrolyte interphase • lithium-sulfur battery • quasi-solid-state mechanism • ultramicroporous carbon

- [1] H. Yamin, E. Peled, *J. Power Sources* **1983**, *9*, 281.
- [2] E. Peled, Y. Sternberg, A. Gorenstein, Y. Lavi, *J. Electrochem. Soc.* **1989**, *136*, 6, <https://doi.org/10.1149/1.2096981>.
- [3] P. G. Bruce, B. Scrosati, J. Tarascon, *Angew. Chem.* **2008**, *47*, 2930.
- [4] A. Manthiram, Y. Fu, S. H. Chung, C. Zu, Y. S. Su, *Chem. Rev.* **2014**, *114*, 11751.
- [5] B. M. Li, J. Lu, *Science* **2020**, *367*, 979.
- [6] R. Cao, W. Xu, D. Lv, J. Xiao, J. Zhang, *Adv. Energy Mater.* **2015**, *5*, 1402273.
- [7] S. Drvarić Talian, G. Kapun, J. Moškon, A. Vizintin, A. Randon-Vitanova, R. Dominko, M. Gaberšček, *Chem. Mater.* **2019**, *31*, 9012.
- [8] S. Li, B. Jin, X. Zhai, H. Li, Q. Jiang, *Chem. Sel.* **2018**, *3*, 2245.
- [9] X. Ji, K. T. Lee, L. F. Nazar, *Nat. Mater.* **2009**, *8*, 500.
- [10] P. Liu, Y. Wang, J. Liu, *J. Energy Chem.* **2019**, *34*, 171.
- [11] M. del C Rojas, M. L. Nieva Lobos, M. L. Para, M. E. González Quijón, O. Cámera, D. Barraco, E. L. Moyano, G. L. Luque, *Biomass Bioenergy* **2021**, *146*, 105971.
- [12] J. Qu, S. Lv, X. Peng, S. Tian, J. Wang, F. Gao, *J. Alloys Compd.* **2016**, *671*, 17.
- [13] S. Chung, P. Han, R. Singhal, V. Kalra, A. Manthiram, *Adv. Energy Mater.* **2015**, *5*, 1500738.
- [14] F. J. García-soriano, M. L. Para, G. L. Luque, D. Barraco, E. P. M. Leiva, G. Lener, *J. Solid State Electrochem.* **2020**, *24*, 2341.
- [15] Z. Zheng, H. Guo, F. Pei, X. Zhang, X. Chen, X. Fang, T. Wang, N. Zheng, *Adv. Funct. Mater.* **2016**, *26*, 8952.
- [16] H. Maria, M. Fichtner, A. Reddy, *J. Energy Chem.* **2021**, *59*, 242.
- [17] J. Gao, M. A. Lowe, Y. Kiya, D. Abrus, *J. Phys. Chem. C* **2011**, *115*, 25132.
- [18] D. Bresser, S. Passerini, B. Scrosati, *Chem. Commun.* **2013**, *49*, 10545.
- [19] S. Urbonaitė, T. Pouk, P. Novák, *Adv. Energy Mater.* **2015**, *5*, 1500118.
- [20] R. Dominko, A. Vizintin, G. Aquilanti, L. Stievano, M. J. Helen, A. R. Munnangi, M. Fichtner, I. Arcon, *J. Electrochem. Soc.* **2018**, *165*, A5014.
- [21] M. Helen, T. Diemant, S. Schindler, R. J. Behm, M. Danzer, U. Kaiser, M. Fichtner, M. Anji Reddy, *ACS Omega* **2018**, *3*, 11290.
- [22] Y. Yin, A. A. Franco, *ACS Appl. Energ. Mater.* **2018**, *1*, 5816.
- [23] S. Xin, L. Gu, N. H. Zhao, Y. X. Yin, L. J. Zhou, Y. G. Guo, L. J. Wan, *J. Am. Chem. Soc.* **2012**, *134*, 18510.
- [24] E. Markevich, G. Salitra, A. Rosenman, Y. Talyosef, F. Chesneau, D. Aurbach, *J. Mater. Chem. A* **2015**, *3*, 19873.
- [25] Y. Xu, Y. Wen, Y. Zhu, K. Gaskell, K. A. Cyhlosz, B. Eichhorn, K. Xu, C. Wang, *Adv. Funct. Mater.* **2015**, *25*, 4312.
- [26] E. Markevich, G. Salitra, Y. Talyosef, F. Chesneau, D. Aurbach, *J. Electrochem. Soc.* **2017**, *164*, A6244.
- [27] D. W. Wang, G. Zhou, F. Li, K. H. Wu, G. Q. Lu, H. M. Cheng, I. R. Gentle, *Phys. Chem. Chem. Phys.* **2012**, *14*, 8703.
- [28] D. W. Wang, Q. Zeng, G. Zhou, L. Yin, F. Li, H. M. Cheng, I. R. Gentle, G. Q. M. Lu, *J. Mater. Chem. A* **2013**, *1*, 9382.
- [29] J. T. Lee, K. Eom, F. Wu, H. Kim, D. C. Lee, B. Zdyrko, G. Yushin, *ACS Energy Lett.* **2016**, *1*, 373.
- [30] E. Markevich, G. Salitra, A. Rosenman, Y. Talyosef, F. Chesneau, D. Aurbach, *Electrochim. Commun.* **2015**, *3*, 19873.
- [31] A. Rosenman, E. Markevich, G. Salitra, Y. Talyosef, F. Chesneau, D. Aurbach, *J. Electrochem. Soc.* **2016**, *163*, 1829.
- [32] E. Markevich, G. Salitra, A. Rosenman, Y. Talyosef, F. Chesneau, D. Aurbach, *J. Mater. Chem. A* **2015**, *3*, 19873.
- [33] A. D. Roberts, X. Li, H. Zhang, *Chem. Soc. Rev.* **2014**, *43*, 4341.
- [34] S.-E. Cheon, K.-S. Ko, J.-H. Cho, S.-W. Kim, E.-Y. Chin, H.-T. Kim, *J. Electrochem. Soc.* **2003**, *150*, A800.
- [35] X. Yang, X. Gao, Q. Sun, S. P. Jand, Y. Yu, Y. Zhao, X. Li, K. Adair, L. Y. Kuo, J. Rohrer, J. Liang, X. Lin, M. N. Banis, Y. Hu, H. Zhang, X. Li, R. Li, H. Zhang, P. Kaghazchi, T. K. Sham, X. Sun, *Adv. Mater.* **2019**, *31*, 1901220.
- [36] S.-E. Cheon, K. Ki-Seok, C. Ji-Hoon, K. Sun-Wook, C. Eog-Yong, K. Hee-Tak, *J. Electrochem. Soc.* **2003**, *150*, A796.
- [37] A. Rosenman, E. Markevich, G. Salitra, D. Aurbach, A. Garsuch, F. F. Chesneau, *Adv. Energy Mater.* **2015**, *5*, 1500212.
- [38] S. Drvarić Talian, J. Bobnar, A. R. Sinigoj, I. Humar, M. Gaberšček, *J. Phys. Chem. C* **2019**, *123*, 27997.

Manuscript received: December 2, 2021

Revised manuscript received: January 25, 2022

Accepted manuscript online: February 7, 2022

Version of record online: February 22, 2022